

Electrical Power From Nanotube and Graphene Electrochemical Thermal Energy Harvesters

Tae June Kang, Shaoli Fang, Mikhail E. Kozlov, Carter S. Haines, Na Li, Yong Hyup Kim,*
Yongsheng Chen, and Ray H. Baughman*

Nanocarbon-based thermocells involving aqueous potassium ferro/ferricyanide electrolyte are investigated as an alternative to conventional thermoelectrics for thermal energy harvesting. The dependencies of power output on thermocell parameters, such as cell orientation, electrode size, electrode spacing, electrolyte concentration and temperature, are examined to provide practical design elements and principles. Observation of thermocell discharge behavior provides an understanding of the three primary internal resistances (i.e., activation, ohmic and mass transport overpotentials). The power output from nanocarbon thermocells is found to be mainly limited by the ohmic resistance of the electrolyte and restrictions on mass transport in the porous nanocarbon electrode due to pore tortuosity. Based on these fundamental studies, a comparison of power generation is conducted using various nanocarbon electrodes, including purified single-walled and multi-walled carbon nanotubes (P-SWNTs and P-MWNTs, respectively), unpurified SWNTs, reduced graphene oxide (RGO) and P-SWNT/RGO composite. The P-SWNT thermocell has the highest specific power generation per electrode weight (6.8 W/kg for a temperature difference of 20 °C), which is comparable to that for the P-MWNT electrode. The RGO thermocell electrode provides a substantially lower specific power generation (3.9 W/kg).

1. Introduction

Power plants and various industrial processes produce large amounts of by-product waste heat. This thermal energy is

Prof. R. H. Baughman
Alan G. MacDiarmid NanoTech Institute
University of Texas at Dallas
Richardson, Texas 75080, USA
E-mail: ray.baughman@utdallas.edu

Dr. T. J. Kang, Prof. Y. H. Kim
School of Mechanical and Aerospace Engineering
Seoul National University
Seoul 151-744, South Korea
E-mail: yongkim@snu.ac.kr

Dr. T. J. Kang, Dr. S. Fang, Dr. M. E. Kozlov, C. S. Haines
Alan G. MacDiarmid NanoTech Institute
University of Texas at Dallas
Richardson, Texas 75080, USA

N. Li, Prof. Y. Chen
Institute of Polymer Chemistry College of Chemistry
Nankai University
Tianjin 300071, China



DOI: 10.1002/adfm.201101639

typically available at temperatures below 100 °C and can only be converted into electricity at relatively low efficiencies.^[1–7] More commonly, waste heat is released to the environment by means of cooling towers or by exchanging thermal energy with river or ocean water. Other examples of utilizing low-grade heat are geothermal energy and solar thermal systems.^[2,8,9]

An alternative conversion process utilizes an electrochemical pathway to provide thermogalvanic energy conversion.^[6,10–16] A thermocell, also known as a thermogalvanic cell, is an electrochemical cell in which electrical energy is generated by the temperature difference between two half-cells. Using an aqueous electrolyte, a thermocell can operate at low temperatures (below 100 °C) to provide a voltage originating from the temperature dependent electrochemical redox potentials of hot and cold electrodes.

Numerous advances have been made in small-scale thermal energy harvesting using thermoelectrics, metal/semiconductor thermocouples, ferromagnetic materials and Stirling engine technology, etc.^[4,17–19] However, physical and material limitations and cost have prevented the wide application of current thermal energy harvesting technology.^[6,17] Despite present low energy conversion efficiencies, thermocells have the potential advantages of simple design, direct thermal-to-electric energy conversion, continuous operation, low expected maintenance, zero carbon emissions and low cost.

Nanocarbon-based thermocells using $\text{Fe}(\text{CN})_6^{4-}/\text{Fe}(\text{CN})_6^{3-}$ aqueous electrolyte are here investigated. The dependence of performance on thermocell parameters, such as cell orientation, electrode size, electrode spacing, electrolyte concentration and temperature, was examined and the discharge behavior of the thermocell was investigated to provide an understanding of the three primary internal resistances that limit output electrical power. Based on these fundamental studies, a comparison of power generation was carried out using various nanocarbon electrodes, including purified single-walled and multi-walled carbon nanotubes (P-SWNTs and P-MWNTs, respectively), unpurified SWNTs, reduced graphene oxide (RGO) and a P-SWNTs/RGO composite.

The goal of the present work is to provide fundamental understanding, rather than to demonstrate a high performance

thermoelectrochemical energy harvesting device. Hence, the inter-electrode separations are large, the used inter-electrode temperature differences are small (20 °C), the electrolyte concentration was low, and no attempt is made at optimizing electrode thickness and structure to provide a vascular structure that can optimize power output. Efforts to provide such initial optimization have been previously described.^[6] The resulting decrease in the number of independent variables enable evaluation of dependences that have been largely ignored in evaluation of the power output of nanocarbon-based thermo-electrochemical energy harvesters. These include the effects of different relative areas of hot and cold electrodes, gravimetrically generated temperature gradients, inter-electrode spacing, and electrode composition for similarly prepared sheets.

2. Theoretical Background

2.1. Principle of Operation

A thermocell is a non-isothermal electrochemical cell used to convert thermal energy directly into electricity. Two nanocarbon electrodes were presently placed at different temperature zones and the electrodes were in contact with electrolyte with or without a permeable membrane interposed in the electrolyte. The inter-electrode temperature difference generates an electrical potential difference because of the temperature dependence of electrode redox potential, even though the electrodes may be identical and immersed in the same solution. When the cell is connected to an external electrical load, the thermally generated potential drives electrons in the external circuit and ions in the electrolyte so that electrical current and power can be delivered. Continuous operation of the thermocell requires diffusion of the reaction product formed at one electrode to the other electrode, where it can then become a reactant.

2.2. Open-Circuit Potential

The thermoelectric potential in a thermocell is generated by the temperature dependence of the free energy difference between reactant and product of a reaction taking place at the electrolyte-electrode interface. The origin of this potential is analogous to that of potentials produced by thermocouples. A minor effect arises from the thermal diffusion potential, which is due to ion migration driven by the temperature difference in the electrolyte (Soret effect).^[10,20,21] However, for most systems of interest, the electrode potentials dominate and the thermal diffusion potential can be neglected for practical purposes, since it is about three orders of magnitude lower than the electrode potential, making only negligible contribution to the total electromotive force (EMF).^[14,22]

Strictly speaking, processes occurring during thermocell power production are not thermodynamically reversible. Therefore, they have been used to develop the theory of thermodynamics of irreversible processes.^[14,22–25] The early literature on thermogalvanic cells is mainly concerned with the dependence of open-circuit potential difference on the

temperature difference between the electrodes.^[10,22,23,25] In particular, the presented theory calculates the thermoelectric coefficient, $\partial E/\partial T$ which represents the temperature dependence of the open-circuit potential produced by the cell. If the redox reaction for a hypothetical redox system ($A + ne \leftrightarrow B$) in the thermocell is given, then the thermoelectric coefficient can be expressed as:

$$nF (\partial E/\partial T)_{t=\infty} = (S_B + \hat{S}_B) - (S_A + \hat{S}_A) - n\bar{S}_e \cong S_B - S_A \quad (1)$$

where n is the number of electrons involved in the above hypothetical redox reaction, F is Faraday constant, the symbols S_A and S_B are the partial molar entropies of species A and B , and their respective Eastman entropies are denoted by \hat{S}_A and \hat{S}_B , accordingly.^[20,21] The Eastman entropy of transport arises from the interaction of an ion and its hydration shell with the solution. Thus, when an ion is transported from one half cell to another in a thermocell system (or is destroyed in one and formed in the other), it carries both its partial molar entropy and the Eastman entropy of transport into the half cell. The sum of these two contributions is often designated as the total transported entropy, which is thus given by $\bar{S}_i = S_i + \hat{S}_i$. The quantity \bar{S}_e is the transported entropy of the electrons in the metallic electrodes and the leads which are maintained at different temperature. This term usually makes only a negligible contribution to $(\partial E/\partial T)_{t=\infty}$, and is typically only 1% of thermocell potential.^[14,22] It should be noted that the subscript ∞ , in Equation 1 implies that sufficient time has been allowed for the system to reach a steady state. Initially, the thermoelectric coefficient is a little (ca. several percent) above the long-term steady-state value. The fall of the initial value is attributed to the Soret effect, which arises because the molecules around the hot electrode diffuse more readily than those around the cold electrode, thus the initially homogeneous solution slowly develops a concentration gradient between the hot electrode and the cold electrode (i.e., the concentration being higher at the cold electrode). The concentration gradient may take even days for the final steady value of $\partial E/\partial T$ to be achieved because the Soret effect is quite small.^[14] Moreover, the transported entropy of the electrons, \bar{S}_e , is also negligible. Therefore it is common to use the initial temperature dependence, which corresponds to deletion of the Eastman entropies of transport and transported entropy of the electrons in Equation 1.

However, the above thermodynamic results for thermocells can only be applied to open-circuit potential conditions—they are not able to predict the discharge behavior when a net current is flowing through a cell as electric power is produced.^[14,22,23] The power output from thermocells depends not only on $\partial E/\partial T$ but also on the current delivery characteristics of the cell (i.e., the three primary internal resistances, such as activation, ohmic and mass transport overpotentials). Experimental measurements may be the only reliable way to determine power generation rates and efficiency of a thermocell. Hence, many observations (such as the time and the output current dependence of the cell potential) can be explained only by incorporating measured electrochemical kinetic parameters into the theoretical analysis.

2.3. Figure of Merit and Power Conversion Efficiency

The efficiency parameter commonly used to describe thermoelectric performance is the figure of merit, Z , which is defined as:^[26]

$$Z = (\partial E/\partial T)^2 \sigma/k \quad (2)$$

where $\partial E/\partial T$ (the thermoelectric coefficient) is the temperature dependence of the inter-electrode potential difference, σ is the electrical conductivity, and k is the thermal conductivity of the electrolyte. Thus, the ratio σ/k shows the relative influence of electrical and thermal conductivities on thermocell operation. Electrical conductivity is mainly attributed to ionic conduction through the electrolyte materials between hot and cold electrodes. Electrolyte thermal conductivity is due to conduction and convection of heat through the redox couple and background solution.

The power conversion efficiency (PCE), Φ , of a thermocell is defined as the ratio of electrical power output (P) from the cell to thermal power flowing ($\partial Q/\partial t$) through the cell:

$$\Phi = P/[kA(\partial T/\partial x) + I\Delta T\Delta S/(nF)] \cong P_{\max}/kA(\partial T/\partial x) \quad (3)$$

The first term in the denominator, $kA(\partial T/\partial x)$, is the rate of heat flow from the hot electrode to the cold electrode and the second term, $I\Delta T\Delta S/(nF)$, is the reversible heat of the cell reaction. The symbol, k , represents the thermal conductivity of the electrolyte, $\partial T/\partial x$ is the temperature gradient between the cell electrodes, and A is the cross-sectional area of the thermocell. The quantities I and ΔT are the current and the absolute temperature differences, respectively. The entropy change for the cell reaction is denoted by ΔS and n is the number of electrons transferred in the cell reaction. Note that inclusion of the reversible heat of reaction, i.e., $I\Delta T\Delta S/(nF)$, in Equation 3 is appropriate only in a thermocell system which involves net consumption of electrolyte. Hence, this term can be eliminated for a thermocell that operates to provide continuous conversion of thermal energy to electricity.

The electrical output power in Equation 3 is commonly expressed as the maximum value, P_{\max} , which occurs when the external load resistance is set equal to the internal resistance of the cell. P_{\max} in Equation 3 can be obtained from experimental characteristic curves of potential difference, E , versus current, I . In the simplest case, in which such $E-I$ curves are linear, it is easy to show that P_{\max} is given by the rectangle of greatest area under the $E-I$ curve. Hence $P_{\max} = 0.25 E_{\text{oc}} I_{\text{sc}}$, where E_{oc} is the open-circuit potential difference and I_{sc} is the short-circuit current delivered by the thermocell. When the $E-I$ characteristic curves are non-linear, P_{\max} can conveniently be determined from the maximum of a graph of $I^2 R$ against R , where R is a variable load resistance.

Finally, the most useful parameter for describing the efficiency of power conversion devices is $\Phi_r(\Phi/\Phi_c)$, the power conversion efficiency relative to that of a Carnot engine. The maximum efficiency for the conversion of heat energy to electrical energy is given by the Carnot expression, $\Phi_c = (T_2 - T_1)/T_2$,

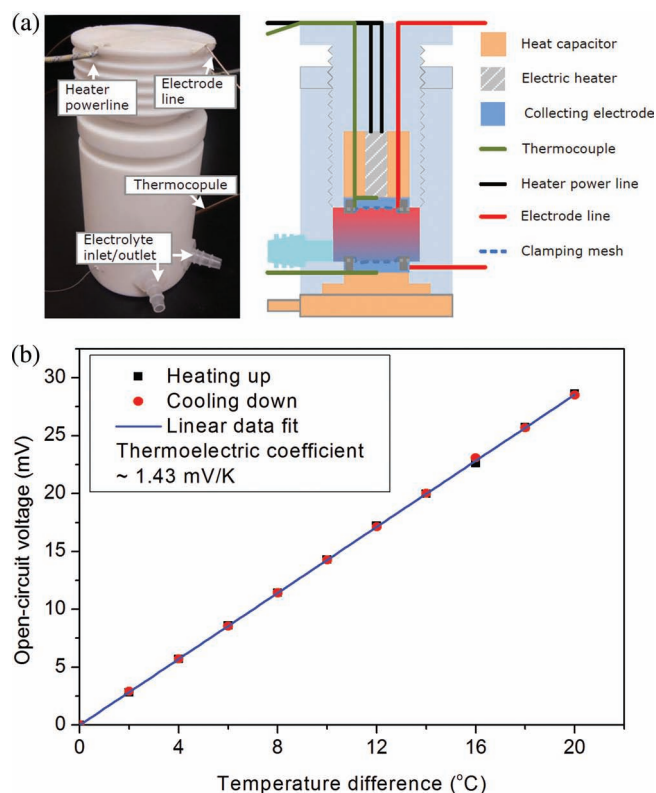


Figure 1. Experimental setup for the thermocell measurements and the results of thermoelectric coefficient measurements for 0.4 M ferro/ferricyanide ($\text{Fe}(\text{CN})_6^{4-}/\text{Fe}(\text{CN})_6^{3-}$) redox couple. a) Schematic drawing of the measurement setup and photograph of the thermoelectrochemical cell. b) The dependence of open-circuit potential on the temperature difference between the hot and cold electrodes. These results are for P-SWNT electrodes with an area of 0.25 cm² and an inter-electrode spacing of 4 cm.

where T_1 and T_2 are the lower and higher absolute temperatures of the respective electrodes.

3. Results and Discussion

3.1. Experimental Setup

Figure 1a shows a schematic diagram and photograph of a thermocell. The hot side temperature was controlled using a resistive heater connected to a temperature controller and the cold side temperature was adjusted by circulating coolant from a thermostatic bath. The cell body with 3 cm internal diameter was constructed from Teflon and the electrode spacing was adjustable in the range from 1 to 7 cm. A glass frit separator was employed at the center of the cell to provide a stable temperature gradient. The temperature of each electrode was monitored using a thermocouple probe. The inter-electrode temperature difference was 20 °C for a cold electrode temperature of 26.4 °C.

A ferro/ferricyanide ($\text{Fe}(\text{CN})_6^{4-}/\text{Fe}(\text{CN})_6^{3-}$) redox couple in water was used as the electrolyte in the thermocell. Various

other redox couples have been proposed for thermocells, such as Cu^{2+}/Cu , Fe^{2+}/Fe , $\text{Pu}^{4+}/\text{Pu}^{3+}$ and $\text{Np}^{4+}/\text{Np}^{3+}$ systems.^[12,15,22,27] Thermocells with the ferro/ferricyanide redox couples have been investigated intensively due to their relatively high thermoelectric power (~ 1.4 mV/K) and the large exchange current density associated with this couple,^[14,15,28] which allows high currents to be drawn from the cell. Furthermore, the ferro/ferricyanide couple is not as vulnerable to electrode poisoning by impurities as compared with other redox couples, such as the $\text{Fe}^{3+}/\text{Fe}^{2+}$ system.^[15]

The thermoelectric coefficient of the ferro/ferricyanide redox couple with a concentration of 0.1 M was investigated by measuring the temperature dependence of the potential difference over a temperature range from 0 to 20 °C with an increment of ± 2 °C. P-SWNT electrodes with an area of 0.25 cm² and electrode spacing of 4 cm were used. As shown in Figure 1b, the measured thermoelectric coefficient (~ 1.43 mV/K) is in good agreement with previous reports (1.4 to 1.6 mV/K).^[15,28–30] Using the measured thermoelectric coefficient and Equation 1, the entropy change for the ferro/ferricyanide reaction is -138 J/mol K.

3.2. Cell Orientation Effect

For continuous thermocell power generation, mass transport is required to transfer reaction product formed at one electrode to the other electrode. Therefore, fast transport of ions is one of the most important parameters for continuously generating high output power. In general, mass transport in thermocells results from both (1) diffusion processes based on electrical potential, thermal gradient (Soret diffusion), and concentration gradient (Fickian diffusion) and (2) convective process based on density gradient. Diffusional transport is relatively slow; however natural convection can be a useful mode of transport in thermocells. The effectiveness of convection in maintaining solution homogeneity may depend on cell orientation and geometrical design; hence these factors may affect the power generation capabilities of the cell. Three types of cell orientations are used in the present study; a thermocell (i) with parallel vertical electrodes (Vertical Hot and Cold), (ii) with horizontal parallel electrodes having the cold electrode above the hot electrode (Cold above Hot), and (iii) with horizontal parallel electrodes but with the hot electrode above the cold electrode (Hot above Cold). For the measurements in Figure 2, SWNT sheet electrodes were tightly clamped between a type 316 stainless plate and fine mesh (woven wire cloth with a mesh size of 58×58 and a wire diameter of 0.045 in.) and attached to the hot and cold sites using thermally conductive but electrically insulating epoxy, and then the cell was completely sealed. The glass frit separator was removed to exclude other effects on transport. SWNT electrodes with an area of 0.25 cm² are utilized, the temperature difference between two electrodes was maintained at 20 °C, the electrode spacing was set to 4 cm and 0.1 M concentration of $\text{Fe}(\text{CN})_6^{4-}/\text{Fe}(\text{CN})_6^{3-}$ redox couple was used. The time needed to collect data for each time coordinate in the resistance plots shown in Figure 2a, c and d was negligible.

It is clear from Figure 2a, c and e that the open-circuit potential is independent of the cell orientation, which is expected if

the open-circuit potential originates from the partial entropy change of redox media. However, short-circuit current and discharge behavior can be significantly affected by the cell orientation. When the “Hot above Cold” orientation is employed, the lower density electrolyte is on top, so convective transport due to the density gradient will be insignificant. In this case the internal resistance, i.e., the slope of $E-I$ curve, continues to increase during cell discharge, reaching steady-state after 10 min (Figure 2a). The maximum electrical output power in steady state was 0.75 μW (Figure 2b). However, in the cases of “Cold above Hot” and “Vertical Hot and Cold” orientations (2c and 2e, respectively) the increase of the internal resistance is relatively small and settles down to a steady state within 60 sec. The steady state internal resistance of the cell is 100 Ω , which is 57% lower than that of the “Hot above Cold” orientation (as shown in the insets of Figure 2c and 2e). Moreover, the maximum output power was increased to 1.8 μW , which is 140% higher than that of the “Hot above Cold” orientation (Figure 2d and 2f). These observations of the internal resistance and the short-circuit current for different orientations can be explained by considering the various types of convection which occur in each case. In particular, the maintenance of a relatively high and steady current generation in the “Cold above Hot” and “Vertical Hot and Cold” orientations is clearly the result of continuous convective mixing which homogenizes the solution so that significant concentration gradients of products and reactants are not formed in the interface between the electrolyte and electrodes. This convective mixing affects the time dependence of internal resistance of the thermocells by contributing to ion transport.

The most important advantage of nanocarbon electrodes is the characteristic high internal surface area, which can increase the number of available reaction sites per unit external area, resulting in increased power density. However, high surface area is by itself not sufficient to guarantee high performance, since actuated fibers having a BET surface area of 2500 m²/g provide poor performance in the electrochemical thermocells.^[6] Highly tortuous ion paths in a nanocarbon electrode may decrease the power density by decreasing ion transport rates within the electrode.^[31,32] Also, such factors as the catalytic properties of the nanocarbon for electron transfer and the electrochemical accessibility of surface can likely not be ignored. The development of an equilibrium concentration in the porous nanocarbon electrode is likely responsible for the time dependence of internal resistance of the thermocells, which has not been observed for platinum electrodes.^[15,33]

The thermocells with “Cold above Hot” and “Vertical Hot and Cold” orientations show similar values in the maximum output power and the internal resistance at steady-state operation. However, “Cold above Hot” orientation shows a slight fluctuation of the internal resistance due to vigorous mixing of electrolyte. Therefore, the “Vertical Hot and Cold” orientation will be used to evaluate cell design parameters in the present study.

3.3. Electrode Size Effect

The capability for power generation in a thermocell is determined by the cell potential and the output current. The cell

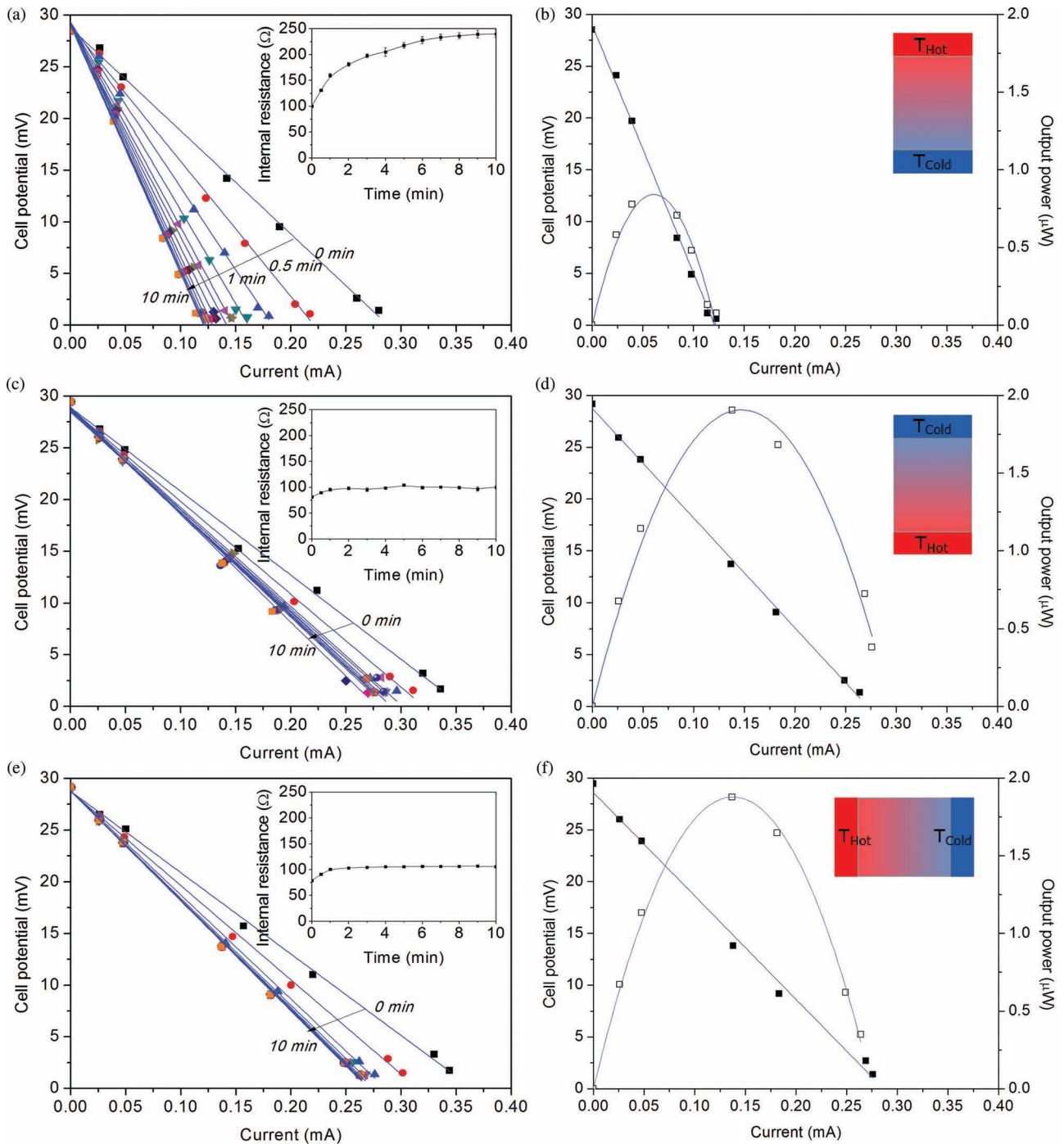


Figure 2. E - I curves, time-variant internal resistance, and output power of SWNT electrode thermocells having different cell orientations. In a) and b) “Hot above Cold”, c) and d) “Cold above Hot”, and e) and f) “Vertical Hot and Cold” orientations were used, respectively. Cell voltage versus cell current at different times from the start of energy harvesting are shown in (a), (c), and (e), where the figure insets show the thereby derived dependence of cell internal resistance on time. b), d), f) The steady state dependence of cell voltage on cell current (solid squares) and the dependence of output power on cell current (open squares).

potential is proportional to the temperature difference and the thermoelectric coefficient of the redox couple. For a given temperature difference, however, the output current may be greatly affected by the internal resistance of the cell. Especially, an increase of electrode size can directly increase the number of

available reaction sites, so that the thermocell generates a higher current, as shown in **Figure 3a**. Increasing the SWNT sheet electrode area from 0.25 to 1.0 cm² increased the short-circuit current from 0.38 to 0.72 mA and increased the maximum power output from 0.4 to 0.74 μW. For the given range of

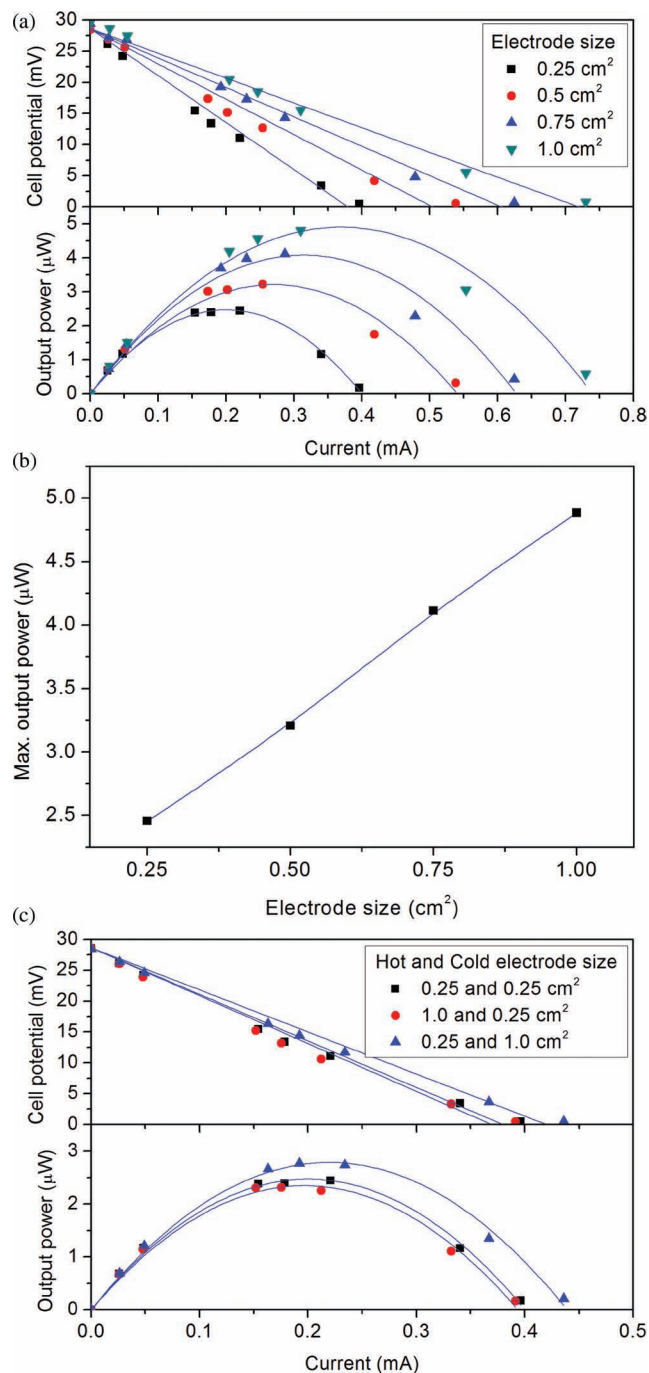


Figure 3. a) Cell voltage and power output versus cell current and b) the maximum power generation as a function of SWNT electrode area when both electrodes have identical area. c) The effect of symmetric and asymmetric sheet areas on the dependence of cell voltage and power generation on cell current. “Vertical Hot and Cold” electrode orientations were used, the temperature difference between the two electrodes was maintained at 20 °C, the inter-electrode spacing was 4 cm, the glass frit separator was employed at the center of the cell and 0.1 M concentration of $\text{Fe}(\text{CN})_6^{4-}/\text{Fe}(\text{CN})_6^{3-}$ redox couple was used.

electrode sizes, a linear relationship between thermocell performance and electrode area is evident from Figure 3b. However, the power does not linearly go to zero when electrode size

approaches zero. It may imply that transport of redox mediator into a porous electrode is limiting currents. The ion transport can be enhanced for a smaller size electrode by increasing ion accessibility through the edges of the SWNT sheet electrode.

Power generation of the thermocell with asymmetric electrode size was evaluated to determine the rate-limiting electrode. As expected, the power generation of the cell was limited by the smaller area electrode and power output was little affected by the size of the larger area counter electrode, as shown in Figure 3c. When the size of the hot electrode was increased 4 times from 0.25 to 1 cm² (to match the area of the cold electrode) there was no significant change in power generation. However, a 4-fold increase in cold electrode area (to match the area of the hot electrode) increased the power output of a thermocell by ~10%. With increasing temperature difference between hot and cold electrodes, the importance of the cold electrode area (relative to the importance of hot electrode area) is expected to increase, since overall redox processes at the two electrodes must be matched to provide a steady state current (and an increased temperature difference reduces the redox rate per electrode surface area for the cold electrode relative to that for the hot electrode).

3.4. Electrode Spacing

The ohmic overpotential in a thermocell is mainly developed by the series resistances of electrode and electrolyte. The resistivity of aqueous electrolyte is generally 2–3 orders of magnitude higher than that of nanocarbon sheets,^[34] thus the ohmic overpotential of thermocell can be dominated by the electrolyte resistance when inter-electrode separations are large. However, the situation is much more complicated, series resistances are also provided by the redox rates for electron transfer at the electrolyte-nanocarbon interfaces and the effect of nanocarbon tortuosity on reducing diffusion of the redox mediator within the electrode

As the electrode spacing between two electrodes decreases, the output power increases due to the decrease of ohmic and mass transport overpotentials as shown in Figure 4a. However, increased input thermal energy is required to maintain the temperature difference between two electrodes because of increased inter-electrode heat transport, which decreases the power conversion efficiency (Figure 4b). The power conversion efficiency is defined by the output electrical power for a given thermal energy flowing into the cell from Equation 3).

3.5. Effect of Electrolyte Concentration

Increasing the concentration of the potassium ferro/ferrocyanide redox couple dramatically decreases cell resistance and increases power output of SWNT thermocells, as is expected from the Butler-Volmer equation.^[12,33] The relationship between cell performance and electrolyte concentration was investigated by changing the concentration of $\text{Fe}(\text{CN})_6^{4-}/\text{Fe}(\text{CN})_6^{3-}$ redox couple from 0.5 mM to 0.2 M. As shown in Figure 5a, the maximum output power increased from 7.6 nW for a 0.5 mM electrolyte to 5.03 μW for a 0.2 M electrolyte. This

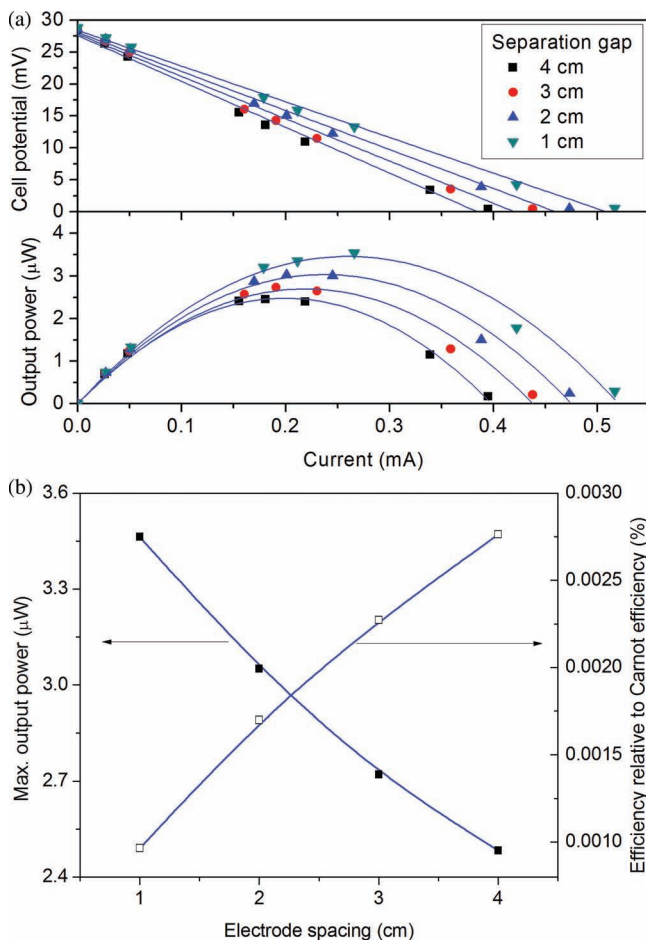


Figure 4. The effects of inter-electrode separation on cell voltage and power output and on cell efficiency for a SWNT thermocell. a) Cell voltage and output power versus cell current for different inter-electrode spacings and b) the maximum power generation and power conversion efficiency as a function of the inter-electrode separation. “Vertical Hot and Cold” electrode orientations were used, the SWNT electrodes had areas of 0.25 cm^2 , the temperature difference between the two electrodes was $20 \text{ }^\circ\text{C}$, the glass frit separator was employed at the center of the cell and 0.1 M concentration of $\text{Fe}(\text{CN})_6^{4-}/\text{Fe}(\text{CN})_6^{3-}$ redox couple was used.

dramatic improvement originates from the increased concentration of redox ions that can react at the electrodes, as well as the increased electrical conductivity of the electrolyte. In a mass transfer controlled electrode reaction, there have been some reports that high concentration of electrolyte may impede ion movement, leading to depletion of reactants (or accumulation of products) at the reaction sites. The mass transport overpotential is prevalent at relatively high current and can decrease power generation in a cell. However, in the present study, it is clear that higher concentration can generate higher power electrical power as shown in Figure 5b.

When we used low concentration of redox mediator in the electrolyte, an increased open-circuit potential was observed and a correspondingly higher thermoelectric coefficient was measured ($1.43 \text{ mV/K} \rightarrow 1.77 \text{ mV/K}$), as shown in Figure 5c. The maximum value of the thermoelectric coefficient can be

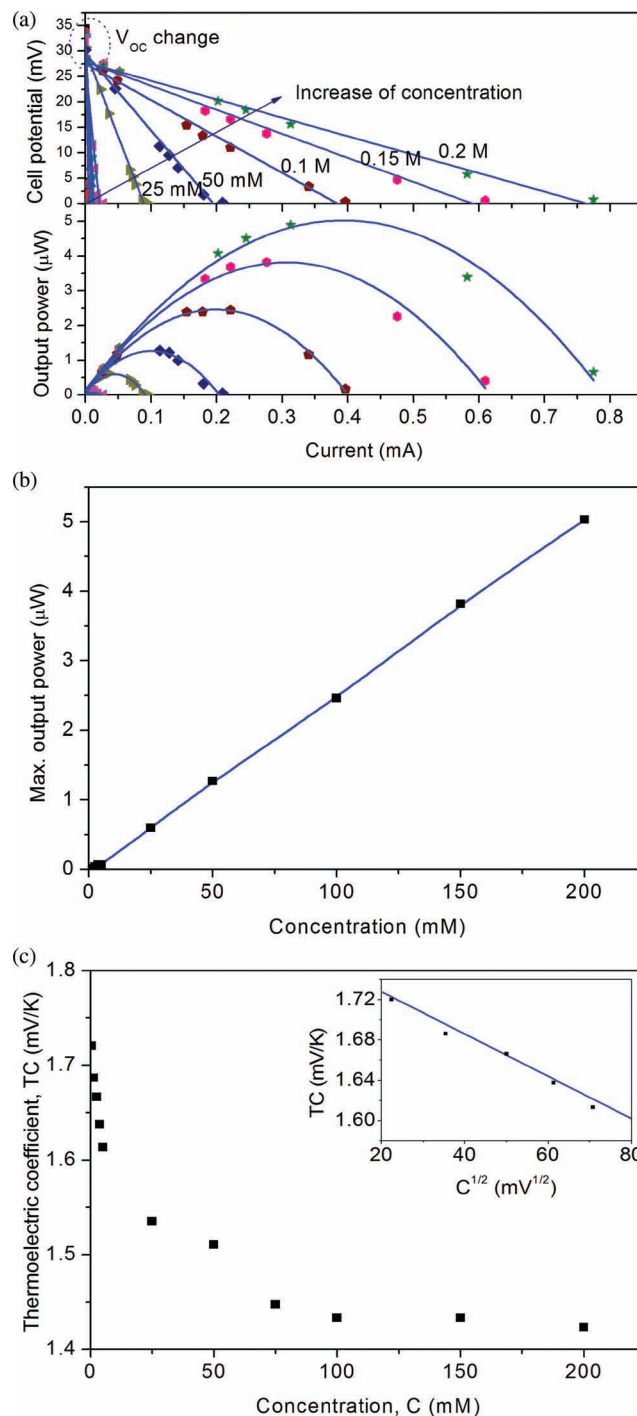


Figure 5. Effect of electrolyte concentration on a) cell voltage and output power versus cell current, b) maximum output power, and c) the Seebeck coefficient for a SWNT thermoelectrochemical cell. “Vertical Hot and Cold” electrode orientations were used, each SWNT electrode had an area of 0.25 cm^2 , the temperature difference between the two electrodes was $20 \text{ }^\circ\text{C}$, the inter-electrode spacing was 4 cm and the glass frit separator was employed at the center of the cell.

attained at infinite dilution, and was 1.72 mV/K for 0.5 mM concentration of the redox mediator. The variation of the thermoelectric coefficient with electrolyte concentration has been

previously reported for other electrodes.^[35–37] The variation is in agreement with a Debye-Hückel treatment of the electrostatic interactions between ions, as shown in the inset of Figure 5c, which predicts a linear variation of the Eastman entropy of transport with the square root of the ionic strength.^[38] However, the generated power is small for low concentrations of the redox mediator. For an electrolyte concentration of over 0.1 M, the thermoelectric coefficient remains constant (~ 1.43 mV/K in Figure 5c), and this thermopower is of interest for practical applications.

3.6. Temperature Effects

The open-circuit potential in a thermocell is basically determined by the temperature difference (ΔT) between the two electrodes, and the proportionality between these two quantities provides the thermoelectric coefficient of the electrolyte. As the temperature difference increases from 5 to 20 °C, the open-circuit potential and output current increase as shown in Figure 6a, resulting in an increase of the maximum power generation from 0.012 μ W for $\Delta T = 5$ °C to 2.47 μ W for $\Delta T = 20$ °C (Figure 6b). It is clear from the results of Figure 1b that the open-circuit potential is linearly proportional to the inter-electrode temperature difference, which is expected from Equation 1. However, the discharge behavior of the thermocell, and therefore the maximum power output, has a more complicated dependence on temperature. If the internal resistance of the cell were largely temperature independent in the relevant temperature range, then power output should increase quadratically with ΔT . However, the data in Figure 6a shows that the slope of cell voltage versus cell current (i.e., the internal resistance of the cell) depends on ΔT . Since the cell internal resistance decreases with increasing ΔT , this means that the power output is enhanced compared with the expected ΔT^2 dependence. Furthermore, even with the same ΔT , the cell internal resistance decreases with increase in the average temperature between the two electrodes (i.e., the operating temperature). More specifically, as the operating temperature increases from 36.4 °C to 46 °C with the same temperature difference of 20 °C, the internal resistance of the cell decreases by 12% (from 71.3 to 62.8 Ω) as shown in Figure 6c.

Increasing the temperature of both electrodes in the thermocell will increase the redox reactivity at these electrodes, as well as increase the ionic conductivity of the electrolyte and diffusion processes within the porous nanocarbon electrodes. Changing the temperature has an exponential effect on the exchange current density as described by the Butler–Volmer equation. Moreover, charge-transfer, ohmic and mass transport resistances can be simultaneously reduced by increasing electrode temperatures.

3.7. Performance Comparison of Various Nanocarbon Materials and Discussion

The purpose of the present section is to compare the performance of various nanocarbons as thermal cell electrodes. Scanning electron microscopy (SEM) images of the nanocarbon electrodes are shown in Figure 7. These nanocarbons

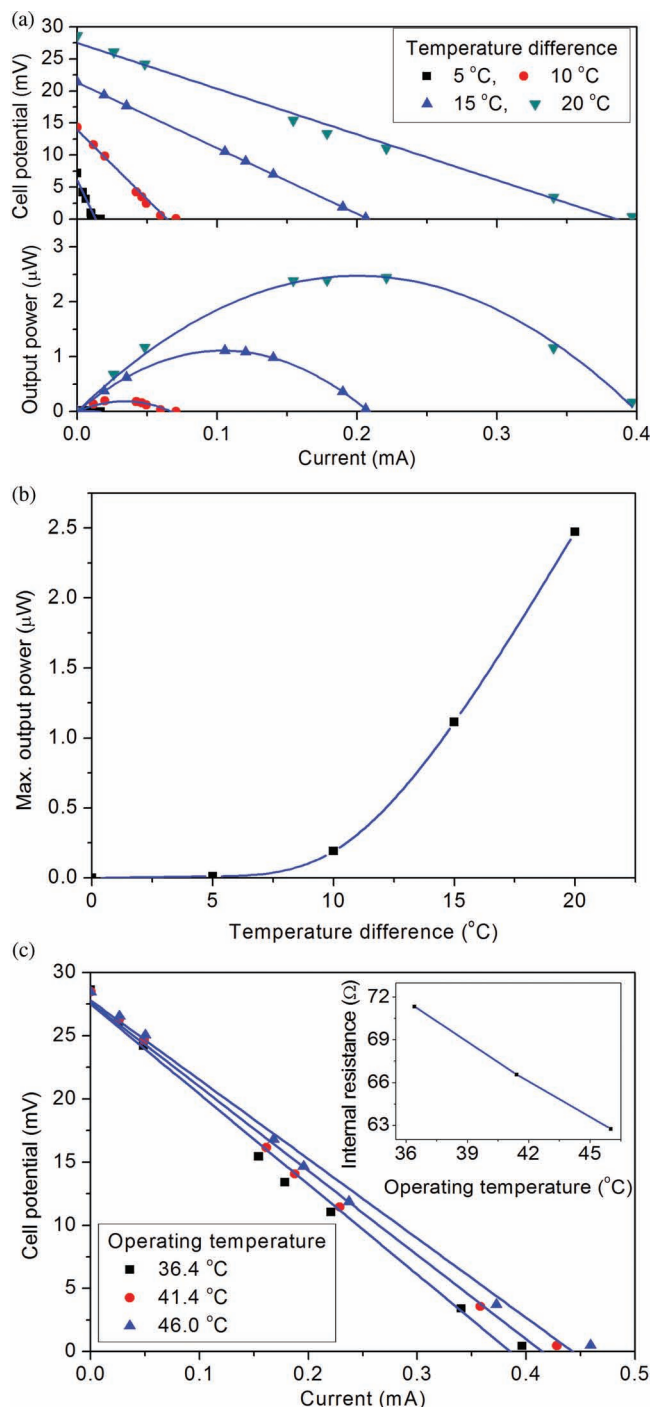


Figure 6. Effect of temperature difference between hot and cold electrodes on a) the dependence of cell potential and output power on output current and b) the maximum power generated. c) The effect of average cell electrode temperature (i.e., operating temperature) on the dependence of cell potential on cell current and the thereby derived internal resistance of the cell for an inter-electrode temperature difference of 20 °C (see insert). “Vertical Hot and Cold” electrode orientations were used, each SWNT electrodes had an area of 0.25 cm², the electrode spacing was 4 cm, the glass frit separator was employed at the center of the cell and a 0.1 M concentration of Fe(CN)₆⁴⁻/Fe(CN)₆³⁻ redox couple was used.

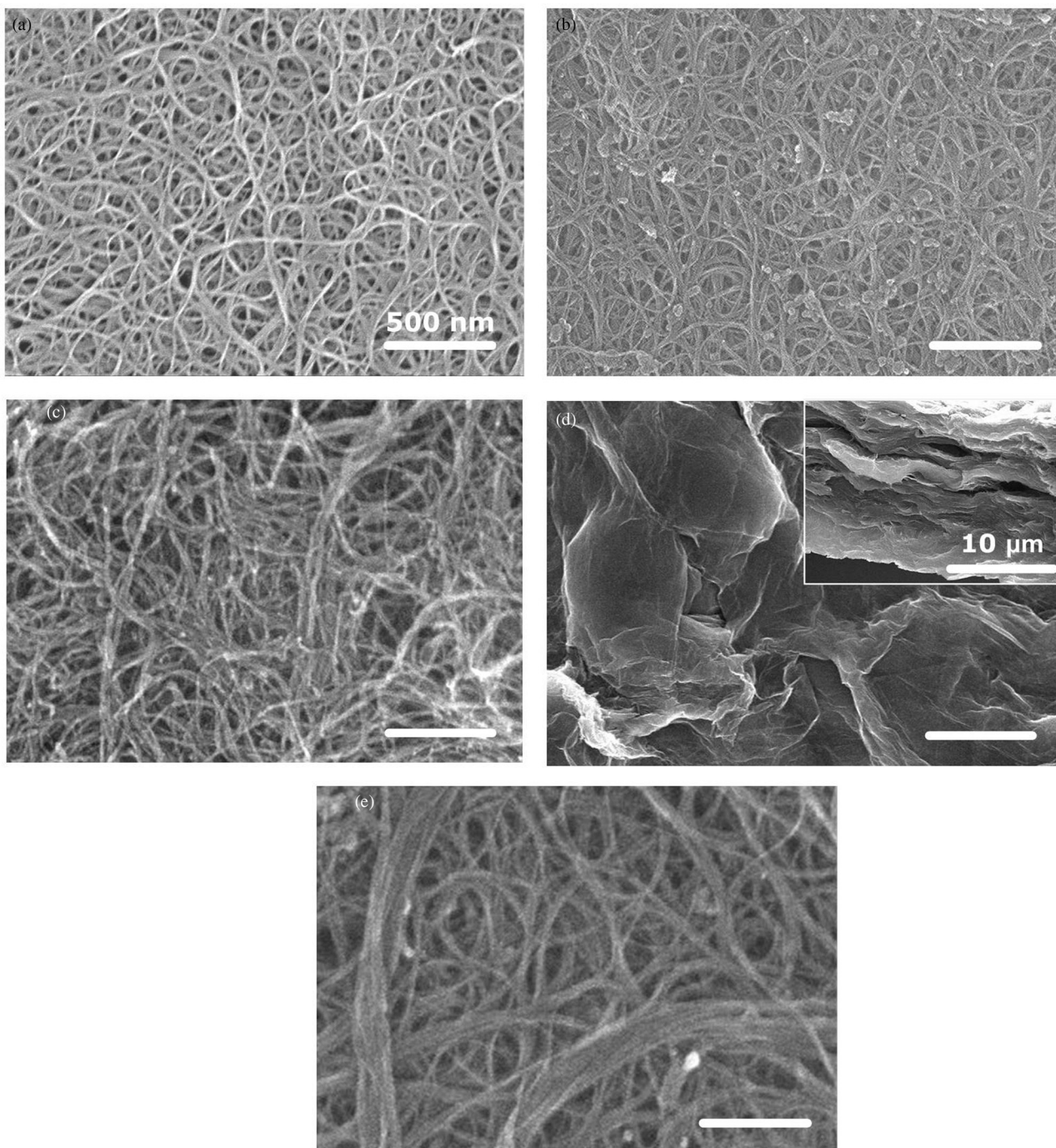


Figure 7. SEM images of nanocarbon electrodes, including a) P-SWNT, b) unpurified SWNT, c) P-MWNT, d) RGO and e) P-SWNT/RGO composite (with identical weight percent of both components). The plate-like layered structure of RGO sheets is clearly shown in the inset of Figure 7d.

(including P-SWNTs, P-MWNTs, unpurified SWNTs, RGO and a P-SWNTs/RGO composite) were used to fabricate thermocell electrodes in the form of sheets via a filtration process. The specific power generation (per one electrode weight) of thermocells based on electrodes of various nanocarbons are shown in **Figure 8** (see also Supporting Information). “Vertical Hot and Cold” electrode orientations were used, the electrode area was 0.25 cm^2 , the temperature difference between two

electrodes was $20 \text{ }^\circ\text{C}$ with a temperature of the cold electrode of $26.4 \text{ }^\circ\text{C}$, the electrode spacing was 4 cm, the glass frit separator was employed and 0.2 M concentration of $\text{Fe}(\text{CN})_6^{4-}/\text{Fe}(\text{CN})_6^{3-}$ redox couple was used.

The thermocells based on a P-SWNT electrode generated a specific power density of $\sim 6.8 \text{ W/kg}$, which is $\sim 32\%$ higher than that obtained for SWNT electrode and $\sim 11\%$ higher than obtained for P-MWNT electrodes. Electrochemical impedance

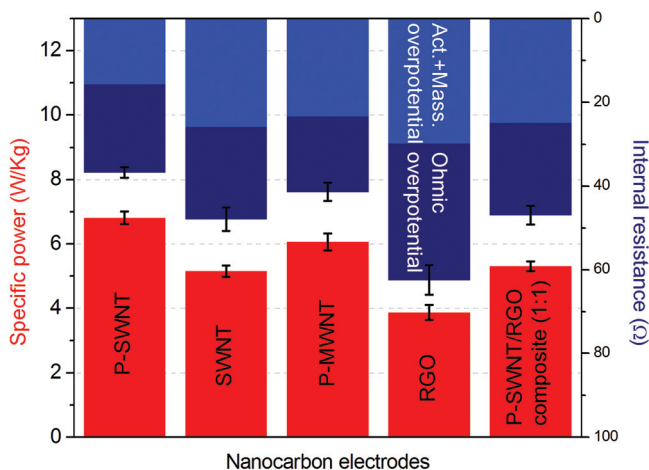


Figure 8. Comparison of power generation by thermocells with nanocarbon electrodes. “Vertical Hot and Cold” electrode orientations were used, the electrode area was 0.25 cm², the temperature difference between the two electrodes was 20 °C, the electrode spacing was 4 cm, a glass frit separator was employed at the center of the cell and 0.2 M concentration of Fe(CN)₆⁴⁻/Fe(CN)₆³⁻ redox couple was used. All errors represent 95% confidence intervals.

spectroscopy (EIS) was used to better understand electrode performance and associated ohmic resistances. The complex plane impedance plots of P-SWNT, SWNT, and P-MWNT electrodes have the general features expected for a porous electrode. The P-SWNT thermocell electrode had a slightly lower ohmic resistance (~21 Ω) than for the unpurified SWNT electrode (~22 Ω) (see Supporting Information). Moreover, the impedance of the purified electrode has a smaller constant phase element compared to the unpurified SWNT electrode at higher frequencies, which indicates enhanced ion penetration in a diffusion-limited electrode.^[39] Hence, the P-SWNT electrodes are expected to provide higher performance in the thermocell than the unpurified SWNT electrode, which is consistent with observations. The P-MWNT thermocell electrode has a lower ohmic resistance (~18 Ω), compared to that for the P-SWNT electrode (~21 Ω), which can result in reduced ohmic overpotential for the thermocell. Apparently, the higher specific surface area for the P-SWNT electrode compensates for the lower resistance of the P-MWNT electrode, thereby providing a slightly higher specific power output for the P-SWNT electrode.

Highly reduced GO sheets and the composite sheets containing 1:1 by weight RGO and P-SWNT were investigated as electrodes for thermocells. RGO is a fascinating material having interesting features such as potentially extremely high specific surface area and unpaired electrons and surface polarizations that can be observed electrochemical experiments.^[40,41] However, the thermocell with the RGO electrode generated a specific power of 3.87 W/kg, which is only ~57% of the specific power generation of the P-SWNT electrode. The ohmic resistance of the RGO thermocell electrode (35.6 Ω, which is ~55% higher than that of the P-SWNT electrode) explains this lower performance of the RGO electrodes. This higher ohmic resistance may be due to the partially irreversible degradation in graphene structure as a result of the oxidation, and incomplete return to

reduced state after reduction. Semicircular impedance response, which typically indicates a resistive electrochemical reaction at the interface, was observed in the EIS study (see Supporting Information), which is consistent with Faradic resistance from residual functional group blocking the reversible electrochemical reaction. Moreover, the plate-like structure RGO sheets (shown in the inset of Figure 7d) is expected to interfere with redox mediator diffusion, so that concentration gradients are amplified inside the RGO electrode. These concentration gradients should decrease power generation in a thermocell because the diffusion flux must exactly balance the reaction flux within the electrode at steady state. Consistent with this hypothesis, the thermocell with a 1:1 weight ratio of P-SWNT and RGO generates ~37% higher specific power (~5.3 W/kg) than the RGO electrode, and shows comparable power generation capability in the thermocell as the SWNT electrode (~5.2 W/kg). This improved performance is likely because the P-SWNTs interfere with the stacking of RGO plates. Since various graphene-based materials derived from GO have quite high capacitances,^[42–44] especially those activated using KOH,^[45] the prospects for using forms of RGO as electrodes for improving thermocell performance are high.

To improve overall thermocell performance, it is important to understand the relationship of discharge behavior to the different sources of internal resistance. Irreversible losses occur during thermocell operation as a result of activation, ohmic and mass transport overpotentials. Activation overpotential represents voltage which is sacrificed to overcome the activation barrier associated with the reactions at the electrode. Various kinetic parameters are important, such as transfer coefficient and exchange current density, which can be analyzed using the Butler–Volmer equation. At the same activation overpotential, higher exchange current density gives a larger net current density. Therefore, improving kinetic performance usually focuses on increasing exchange current density. Utilizing an increased number of possible reaction sites (Figure 3), higher reactant concentration (Figure 5) and increasing the temperature difference and operating temperature (Figure 6) can improve the exchange current density between the nanocarbon electrode and electrolyte. Decreasing the activation barrier can be achieved by using a catalytic electrode, such as possibly a nitrogen-doped CNT electrode. However, the various nanocarbon electrode materials in the present study generally have low activation overpotential between the electrodes and the ferro/ferricyanide in aqueous electrolyte, giving fast electron transfer characteristics and a quasi-reversible reaction.^[6,41,46] Especially noteworthy, a MWNT sheet shows three times higher charging current density during CV scans than a platinum electrode with the same external sheet area.^[6] Therefore, the most effective approaches for improving the thermocell performance would be reducing the ohmic and mass transport overpotentials shown in Figure 8.

Ohmic overpotential occurs due to resistive loss in the cell. The ionic contribution to ohmic resistance tends to dominate in nanocarbon electrode thermocells, rather than the resistance of the electrode material, as described in Figure 4. Since the resistance obeys Ohm’s law, the amount of voltage lost in order to force ion conduction varies linearly throughout the electrolyte. Therefore decreasing the electrode spacing, i.e., thin

thermocells, can improve power generation even though the power conversion efficiency of the cell will be decreased. The cell orientation, operating temperature, and electrolyte concentrations can also affect the ohmic overpotential.

Mass transport or concentration polarization results when the electrode reactions are hindered by mass transfer effects. The mass transport process is needed to transport the reaction product formed at one electrode to the other electrode for continuous operation in a thermocell. As soon as the thermocell begins producing current, the electrochemical reaction leads to depletion of reactants (and accumulation of products) at the electrode. Then, the reactant and product concentration profiles drop linearly with distance across the electrode, i.e., diffusion layer, at steady state. The mass transport overpotential is generally prevalent at relatively high current discharge in an electrochemical cell; however, the development of a concentration profile can be significant in nanocarbon based thermocells due to highly porous and tortuous electrode structures (see also the time-variant internal resistance change as shown in Figure 2). Therefore, an electrode structure with low tortuosity as well as high surface area is highly desired to provide high power generation for the nanocarbon electrode thermocells.

Various methods have been proposed for the conversion of waste heat to electrical, mechanical, or chemical energy and for the useful storage of waste heat.^[3,6–10,47] Of these methods, thermoelectric conversion of waste heat to electrical energy is especially attractive.

While semiconductor-based solid-state thermoelectrics can reach at least ~20% of Carnot efficiency, the power conversion efficiencies of thermocells are presently no higher than about ~1.4% of Carnot efficiency (obtained for thermocells based on MWNT electrodes, which were operated with a ΔT of ~60 °C using the $\text{Fe}(\text{CN})_6^{4-}/\text{Fe}(\text{CN})_6^{3-}$ redox couple^[6]). While major increases in the power conversion efficiencies are possible, based on increase of the effective thermo-electrochemical Seebeck coefficient and the ratio of ionic conductivity to thermal conductivity, it seems doubtful that electrochemical will ever exceed the thermal energy conversion efficiencies achievable for solid-state thermoelectrics. However, conventional solid-state thermoelectrics are expensive and inflexible, so they seem unsuitable for such applications as wrapping around a hot pipe that exits a chemical plant. In these applications, and many others where the thermal energy would otherwise be lost, the target is to maximize energy output as expressed as Wh/dollar, and in this regime the electrochemical thermal cells might have major advantages (as suggested in a very preliminary way by previous comparisons of Wh/dollar of solar and electrochemical thermocells.^[6])

4. Conclusions

In summary, nanocarbon electrode thermocells with potassium ferrocyanide aqueous electrolyte have been investigated for harvesting low grade thermal energy. The performance dependency on thermocell parameters, such as cell orientation, electrode size, electrode spacing, concentration of electrolyte and temperature was examined. The discharge behavior of the thermocell was also investigated, resulting in an understanding

of the three primary internal resistances. Based on these fundamental studies, a comparison of power generation was carried out using various nanocarbon materials. The power output from the nanocarbon thermocells was found to be mainly limited by the ohmic resistance of the electrolyte and the mass transport in a porous nanocarbon electrode due to high tortuosity of the pore structure. Thin thermocells with low ohmic overpotential can be promising candidates to improve power generation from waste thermal energy. Especially, a nanocarbon electrode structure with low tortuosity as well as high surface area is highly desirable to provide high power generation for the nanocarbon electrode thermocells. The nanocarbon thermocell may become an attractive alternative for harvesting low-grade heat, given their simple design, direct thermal to electric energy conversion, continuous operation, low expected maintenance, and zero carbon emission.

5. Experimental Section

Material Preparation: The origins and characteristics of the carbon nanotubes used for electrode fabrication are as follows: The unpurified SWNT powders (ASA-100F, Hanwha Nanotech) were produced by arc discharge, had an average nanotube diameter of ~1.3 nm and low purity (comprising 20–30 wt.% nanotubes, 40 wt.% of carbon nanoparticles, 20 wt.% of catalyst metal, and 10 wt.% of amorphous carbon and graphite).^[48] P-SWNT powders (ASP-100F, Hanwha Nanotech) were commercially purified by thermal and acid treatments of ASA-100F. After purification, this product has a nanotube content of 60–70 wt.% and contains approximately 10 wt.% of metal catalyst and 20 wt.% of graphitic impurities. The P-MWNT powder (SMW100, SouthWest NanoTechnologies, Inc.) contains approximately 98 wt.% carbon, mostly as MWNTs containing 3 to 6 walls that have a median diameter of 6.6 nm.

Nanocarbon materials, including purified P-SWNT, P-MWNT, unpurified SWNT, RGO and P-SWNT/RGO composite (with identical weight percent of both components) were used to fabricate thermocell electrodes in the form of sheets via a filtration process. This involved vacuum filtering a nanocarbon suspension in anhydrous *N,N*-dimethylformamide (*N,N*-DMF, Sigma Aldrich) onto a membrane filter (Millipore PTFE filter, 0.2 μm pore size, 47 mm diameter), washing with deionized (DI) water and methanol, drying in vacuum, and removal of the formed sheet from the filter.

Graphene oxide (GO) was synthesized using a modified Hummers method.^[40,49] In this process 300 mg of graphite flakes (GF, Sigma Aldrich) were dispersed in 36 mL of sulfuric acid (H_2SO_4) and stirred for an hour. Afterwards, 4 mL of phosphoric acid (H_3PO_4) was added to the solution and stirred for 15 min. This addition of phosphoric acid facilitated the ultimate production of graphene oxide having decreased disruption of the graphitic basal planes. Then, 1.8 g (600 wt.%, relative to the 300 mg GF) of potassium permanganate (KMnO_4) was added as an oxidizing agent and the solution was stirred at 50 °C for 12 h. After the oxidation process, the solution was placed in an ice bath and 15 mL of hydrogen peroxide (H_2O_2) was added and stirred for 5 min. This GO dispersion was subjected to vacuum filtration and the GO was collected on the membrane filter. To remove manganese dioxide (MnO_2) present as a by-product of oxidation, the GO sheet was re-dispersed in hydrogen chloride (HCl) and was filter-collected as before. Finally, the collected GO sheet was washed with methanol and DI water until neutral pH was obtained.

The solvent (anhydrous *N,N*-DMF) used to obtain nanocarbon sheet electrodes is well-known medium for the dispersion of CNTs and RGO.^[40,50] The CNT powders were added into *N,N*-DMF to produce a concentration of 0.2 mg/mL, which could be readily dispersed by sonication for 5 h to debundle the CNTs. Then the CNTs were collected on a membrane filter, using vacuum filtration, and washed successively

with DI water and methanol. The CNT sheet electrode was then removed from the filter and dried in a vacuum oven at 80 °C for 48 h.

The preparation of RGO dispersion was carried out using the reported procedure.^[40] Briefly, the GO produced by the above described method was added to water to produce 3.0 mg GO/mL water mixture, which was bath sonication for 1 h to obtain dispersion. Then, N,N-DMF solution was added to the dispersion to produce a 9:1 volume ratio of N,N-DMF and water, resulting in a concentration of 0.3 mg GO/mL. Chemical reduction of the suspension of GO sheets was accomplished using hydrazine monohydrate (N₂H₄·H₂O) (1 μL/3 mg GO) for 12 h at 80 °C with stirring, creating a homogeneous black suspension. The resulting suspension was neutral to a pH of ~7. The agglomerated particles could be re-dispersed with a short sonication of less than 5 min. After the preparation of RGO suspension, the RGO was collected on a membrane filter and dried in a vacuum oven chamber in the same manner as the CNT materials. However, chemical reduction using hydrazine may not be sufficient to fully reduce GO due to the presence of the hydroxyl, carbonyl, and carboxyl groups.^[41,51] Therefore, thermal annealing was additionally used to effectively reduce GO sheets. Thermal reduction of the GO paper was carried out under 5% hydrogen in argon gas using the following temperature profile: 20–900 °C at 10 °C/min, 900 °C for 1 hour, and cooling down to room temperature overnight.

Various aqueous 1:1 concentrations of potassium ferricyanide (K₃Fe(CN)₆, Sigma Aldrich) and potassium ferrocyanide (K₄Fe(CN)₆·3H₂O, Sigma Aldrich) electrolyte solutions were used for the thermocells. Provided concentrations here and elsewhere are total molar concentrations. All solutions were prepared using water from a high purity deionization system (Millipore, milli-Q Water Purification System) and were degassed before use by bath sonication. The effects of any long-term decomposition of stock solution were monitored for a period of over three weeks, by measuring the performance of cells fabricated using aged dispersions, and performance degradation was found to be negligible when electrolyte with relatively low total concentration (<0.1 M) was used. However, some decomposition and aggregation was observed at a higher concentration, especially 0.4 M, which is close to saturation. To avoid the effect of electrolyte degradation, the freshly prepared electrolytes were immediately incorporated into the thermogalvanic cell before the commencement of a series of measurements.

Instrumental: All nanocarbon electrodes were formed into 30 μm thick sheets (to place performance comparisons on the same scale, when normalized to sheet area). These electrodes were connected to a 0.5 mm diameter platinum (Pt) wire using silver paste, which was used to minimize contact resistance. The contact was then covered by insulating paint to prevent possible artifacts due to interaction between the silver paste and the electrolyte. The potential and current output from the cell was measured using a voltage–current meter (Keithley 2000 multimeter) with 0.002% DC voltage accuracy from 100 nV to 1 kV. Electrode temperatures were measured using thermocouple probes (Sper Scientific, Type K) that were placed close to each electrode. A standard load resistor array (Tenma 72-7270) was used for characterizing power output versus resistive load. A conventional three-electrode cell was used for all electrochemical experiments that complemented measurements for the complete thermocell. The working electrode was a 0.25 cm² area sheet of nanocarbon electrode, the reference electrode was Ag/AgCl stored in 3.0 M NaCl, and the auxiliary electrode consisted of a sheet of Pt foil that was several times larger in area than the working electrode. The cyclic voltammetry (CV) data was obtained using a potentiostat (Gamry Potentiostat, v4.35) and cell impedance measurements as a function of the frequency of applied AC potential were conducted using a commercially available instrument (EIS, Gamry Echem Analyst, v5.5).

Supporting Information

Supporting Information is available from the Wiley Online Library or from the author.

Acknowledgements

This research was supported by the National Research Foundation of Korea (grants No. 2009-0083512, No. 2010-0018736 and No. 2010-0000786), the second stage of the Brain Korea 21 Project in 2010, Air Force grant FA9550-11-C-0061, a grant from the National Science Foundation supported Center for Energy Harvesting Materials and Systems, and Robert A. Welch Foundation Grant AT-0029. The authors also acknowledge support from the Institute of Advanced Aerospace Technology at Seoul National University.

Received: July 16, 2011

Revised: September 28, 2011

Published online: December 6, 2011

- [1] J. A. Turner, *Science* **1999**, *285*, 687.
- [2] I. Dincer, *Energy Build.* **2002**, *34*, 377.
- [3] J. A. Paradiso, T. Starner, *IEEE Pervasive Comput.* **2005**, *4*, 18.
- [4] M. Ujihara, G. P. Carman, D. G. Lee, *Appl. Phys. Lett.* **2007**, *91*, 093508.
- [5] L. E. Bell, *Science* **2008**, *321*, 1457.
- [6] R. Hu, B. A. Cola, N. Haram, J. N. Barisci, S. Lee, S. Stoughton, G. Wallace, C. Too, M. Thomas, A. Gestos, M. E. d. Cruz, J. P. Ferraris, A. A. Zakhidov, R. H. Baughman, *Nano Lett.* **2010**, *10*, 838.
- [7] Y. Ito, T. Nohira, *Electrochim. Acta* **2000**, *45*, 2611.
- [8] R. Shinnar, F. Citro, *Technol. Soc.* **2007**, *29*, 261.
- [9] R. H. Hammond, W. M. Risen Jr., *Sol. Energy* **1979**, *23*, 443.
- [10] H. Levin, C. F. Bonilla, *J. Electrochem. Soc.* **1951**, *98*, 388.
- [11] D. H. Angell, T. Dickinson, *J. Electroanal. Chem.* **1972**, *35*, 55.
- [12] B. Burrows, *J. Electrochem. Soc.* **1976**, *123*, 154.
- [13] T. Ikeshoji, S. K. Ratkje, *J. Electrochem. Soc.* **1986**, *133*, 1107.
- [14] T. I. Quickenden, C. F. Vernon, *Sol. Energy* **1986**, *36*, 63.
- [15] T. I. Quickenden, Y. Mua, *J. Electrochem. Soc.* **1995**, *142*, 3985.
- [16] Y. Ito, R. Takeda, S. Yoshizawa, Y. Ogata, *J. Appl. Electrochem.* **1985**, *15*, 209.
- [17] C. B. Vining, *Nat. Mater.* **2009**, *8*, 83.
- [18] A. Khaligh, Z. Peng, Z. Cong, *IEEE Trans. Ind. Electron.* **2010**, *57*, 850.
- [19] J. Tang, H.-T. Wang, D. H. Lee, M. Fardy, Z. Huo, T. P. Russell, P. Yang, *Nano Lett.* **2010**, *10*, 4279.
- [20] E. D. Eastman, *J. Am. Chem. Soc.* **1926**, *48*, 1482.
- [21] E. D. Eastman, *J. Am. Chem. Soc.* **1928**, *50*, 283.
- [22] A. J. de Bethune, T. S. Licht, N. Swendeman, *J. Electrochem. Soc.* **1959**, *106*, 616.
- [23] P. D. Miller, J. Arch B. Tripler, J. J. Ward, *J. Electrochem. Soc.* **1966**, *113*, 746.
- [24] J. N. Agar, C. Y. Mou, J. L. Lin, *J. Phys. Chem.* **1989**, *93*, 2079.
- [25] J. Newman, *Ind. Eng. Chem. Res.* **1995**, *34*, 3208.
- [26] R. Venkatasubramanian, E. Siivola, T. Colpitts, B. O'Quinn, *Nature* **2001**, *413*, 597.
- [27] P. Blanc, C. Madic, *Inorg. Chim. Acta.* **1984**, *95*, 141.
- [28] T. Hirai, K. Shindo, T. Ogata, *J. Electrochem. Soc.* **1996**, *143*, 1305.
- [29] Y. Mua, T. I. Quickenden, *J. Electrochem. Soc.* **1996**, *143*, 2558.
- [30] K. B. Koller, F. M. Hawkridge, *J. Am. Chem. Soc.* **1985**, *107*, 7412.
- [31] S. M. Cooper, H. F. Chuang, M. Cinke, B. A. Cruden, M. Meyyappan, *Nano Lett.* **2003**, *3*, 189.
- [32] L. F. Dumée, K. Sears, J. Schütz, N. Finn, C. Huynh, S. Hawkins, M. Duke, S. Gray, *J. Membr. Sci.* **2010**, *351*, 36.
- [33] T. I. Quickenden, Y. Mua, *J. Electrochem. Soc.* **1995**, *142*, 3652.
- [34] R. Reddy, *J. Phase Equilib. Diffus.* **2006**, *27*, 210.
- [35] Y. V. Kuz'minskii, A. A. Andriiko, *J. Electroanal. Chem.* **1988**, *252*, 39.

- [36] Y. V. Kuz'minskii, A. V. Gorodyskii, *J. Electroanal. Chem.* **1988**, 252, 21.
- [37] Y. V. Kuz'minskii, V. A. Zasukha, G. Y. Kuz'minskaya, *J. Power Sources* **1994**, 52, 231.
- [38] E. Helfand, J. G. Kirkwood, *J. Chem. Phys.* **1960**, 32, 857.
- [39] H.-K. Song, H.-Y. Hwang, K.-H. Lee, L. H. Dao, *Electrochim. Acta* **2000**, 45, 2241.
- [40] S. Park, J. An, I. Jung, R. D. Piner, S. J. An, X. Li, A. Velamakanni, R. S. Ruoff, *Nano Lett.* **2009**, 9, 1593.
- [41] L. Tang, Y. Wang, Y. Li, H. Feng, J. Lu, J. Li, *Adv. Funct. Mater.* **2009**, 19, 2782.
- [42] Y. Wang, Z. Shi, Y. Huang, Y. Ma, C. Wang, M. Chen, Y. Chen, *J. Phys. Chem. C* **2009**, 113, 13103.
- [43] W. Lv, D. M. Tang, Y. B. He, C. H. You, Z. Q. Shi, X. C. Chen, C. M. Chen, P. X. Hou, C. Liu, Q. H. Yang, *ACS Nano* **2009**, 3, 3730.
- [44] Y. Zhu, M. D. Stoller, W. Cai, A. Velamakanni, R. D. Piner, D. Chen, R. S. Ruoff, *ACS Nano* **2010**, 4, 1227.
- [45] Y. Zhu, S. Murali, M. D. Stoller, K. J. Ganesh, W. Cai, P. J. Ferreira, A. Pirkle, R. M. Wallace, K. A. Cychosz, M. Thommes, D. Su, E. A. Stach, R. S. Ruoff, *Science* **2011**, 332, 1537.
- [46] J. M. Nugent, K. S. V. Santhanam, A. Rubio, P. M. Ajayan, *Nano Lett.* **2001**, 1, 87.
- [47] F. J. DiSalvo, *Science*. **1999**, 285, 703.
- [48] T. J. Kang, M. Cha, E. Y. Jang, J. Shin, H. U. Im, Y. Kim, J. Lee, Y. H. Kim, *Adv. Mater.* **2008**, 20, 3131.
- [49] D. C. Marcano, D. V. Kosynkin, J. M. Berlin, A. Sinitskii, Z. Sun, A. Slesarev, L. B. Alemany, W. Lu, J. M. Tour, *ACS Nano* **2010**, 4, 4806.
- [50] S. D. Bergin, Z. Sun, D. Rickard, P. V. Streich, J. P. Hamilton, J. N. Coleman, *ACS Nano* **2009**, 3, 2340.
- [51] X. Gao, J. Jang, S. Nagase, *J. Phys. Chem. C* **2009**, 114, 832.